Journal of Power Sources 190 (2009) 545–552

Contents lists available at ScienceDirect

Journal of Power Sources

journal homepage: www.elsevier.com/locate/jpowsour

Lithium ion intercalation in partially crystalline TiO_2 electrodeposited on platinum from aqueous solution of titanium(IV) oxalate complexes

Paweł Marek Dziewoński[1], Maria Grzeszczuk*

Faculty of Chemistry, University of Wrocław, 14 F. Joliot-Curie street, 50-383 Wrocław, Poland

ARTICLE INFO

Article history:
Received 17 October 2008
Received in revised form 8 December 2008
Accepted 18 January 2009
Available online 23 February 2009

Keywords:
Titanium(IV) oxide
Li^+ intercalation
Cyclic electrodeposition
Impedance analysis

ABSTRACT

Starting from the aqueous solution of titanium(IV) oxalate complexes and controlling electrochemical conditions using a cyclic voltammetry (CV) method, the thin layers of TiO_2 on platinum were obtained, which after additional heat treatment, at 450 °C, were still of amorphous nature. The amorphous state of the samples, containing an admixture of crystalline anatase, was confirmed by Raman spectroscopy and by a variety of electrochemical techniques. The new electrochemical procedure allows preparing the oxide with different morphologies. By the comparison with the peroxotitanium route, the oxalate precursor method offers the possibility of the synthesis of amorphous TiO_2 at higher temperatures that is the essential key for the cycling stability of the oxide if one is used as an anode material in lithium ion batteries. The results from cycling voltammetry revealed that electrodeposited TiO_2 reversibly and fast intercalates lithium ions due to its high internal surface area. Therefore, the nanostructural morphology facilitates lithium ion intercalation which was monitored and confirmed in all electrochemical testing. The specific capacity of the TiO_2 approaches the value of 145 mAh g^{-1} at 8 C-rate in the best case. From the electrochemical impedance spectroscopy (EIS) measurements in connection with SEM investigations, it was concluded that Li^+ diffusion is the finite space process and its rate is depending on the size of the crystallites building the oxide films. Evaluated values of the *D*-coefficients are of the order of 10^{-14} cm^2 s^{-1}.

1. Introduction

Titanium(IV) oxide, as many other oxides of the transition metals, is able to intercalate small ions like H^+, Li^+, and even Na^+ as well [1]. The process can be described by the following equation:

$$TiO_2 + xLi^+ + xe^- \leftrightarrows Li_xTiO_2 \quad (1)$$

The intercalation has already been studied for the different polymorphic forms of TiO_2. In the case of anatase, the intercalation degree *x* was usually equal 0.5 [2]. It corresponds to a quite high value of the specific capacity, 168 mAh g^{-1}, reached at the rather low electrode potentials, around 1.5/1.6 V *vs.* Li/Li^+. Anatase is considered as a very good material for electrochromic devices [3] and the anode in lithium ion batteries where it can substitute graphite [4–6].

New improvements in the intercalation properties of TiO_2 are still expected. It is known that even small changes in procedures of the synthesis result in meaningful changes in of the *x*-coefficient value as well as reversibility, stability and the intercalation rate of the oxide material [7]. The most important factors for the properties are polymorphic form of TiO_2, the morphology of the oxide phase [8,9], sizes/geometry of the crystallites and their distribution [10], mesomicroporosity [11]. It should be noted that the electrochemical procedures are reported to lead usually to the worse properties of TiO_2 than other methods [12]. The highest capacity under the high current loads and charging rate were found for nanotubular TiO_2, *i.e.* 300 and 100 mAh g^{-1} at the C-rate 0.06 and 18 C, respectively [13].

Rutile, characterized by the most compact structure among the polymorphic forms of TiO_2, intercalates Li^+ the least easily. Interestingly, rutile-like RuO_2, having nearly identical elemental cell dimensions, is able to accommodate Li^+ to a high level of $x = 1.3$, that can be due to the electronic conductivity of this oxide [14]. Thus, an increase in the conductivity by, for example, forming composites of the oxide with good electronic conductors can be a method for an improvement of the TiO_2 intercalation ability [15]. An another strategy would be to use the amorphous oxide due to its rather low tendency to undergo the mechanical defects when working in the cyclic regimes. It was found to give the satisfactory properties also for TiO_2 [16]. On the other hand, the chemical composition of the Ti(IV) solution is of a foremost importance for the oxide deposited on the electrode. The worse electrochemical properties of amorphous TiO_2, prepared from titanium peroxocomplexes, as compared with crystalline anatase have been described as due to higher water content in the former material [17].

* Corresponding author. Tel.: +48 71 3757336.
E-mail address: maria@wchuwr.pl (M. Grzeszczuk).
[1] Presented at "XI Symposium on Fast Ionic Conductors", Grybów, Poland, 14–17 September 2008.

0378-7753/$ – see front matter © 2009 Elsevier B.V. All rights reserved.
doi:10.1016/j.jpowsour.2009.01.041

Our results on the Li^+ intercalation in the partially crystalline titanium(IV) oxide containing anatase are presented in this paper. The oxide material was obtained from Ti(IV) oxalate complexes by means of a new cyclic electrodeposition procedure. The oxalate media lead to the partly crystalline oxide with the lower water content due to the higher temperatures, by 150 °C, of heat treatment than used for the peroxotitanium route. Furthermore, some effects of the morphology of the electrodeposited oxide films on the Li^+ intercalation process are reported in this work.

2. Experimental

2.1. Electrochemical experiments

All electrochemical measurements were performed in a conventional three-electrode cell using the Solartron Analytical 1287 electrochemical interface coupled with the 1260 impedance/gain-phase analyzer. Depending on the solvent, the potentials in this work were referred to a saturated calomel electrode (SCE) or a home-made silver/silver ion electrode for water or propylene carbonate (PC)-based electrolyte systems, respectively. The silver/silver ion electrode (Ag/0.01 M $AgClO_4$ (Alfa Aesar, 99.9%) in 1 M $LiClO_4$-PC) was calibrated against SCE after determining the formal potentials of the ferroceniumdimethanol/ferrocenedimethanol internal standard couple in 1 M aqueous or propylene carbonate $LiClO_4$ solutions by means of cycling voltammetry. On the assumption that the activity coefficient of lithium cation in 1 M $LiClO_4$-propylene carbonate solution is equal to 1, the potentials in the silver/silver ion scale were recalculated to the lithium/lithium ion scale according to the equation:

$$E(\text{Li/1 M LiClO}_4\text{-PC}) = E(\text{Ag/0.01 M AgClO}_4 \text{ in 1 M LiClO}_4\text{-PC}) + 3.79\,(\text{V}) \quad (2)$$

The lithium/lithium scale potentials will be quoted in parentheses when necessary for a comparison with the literature data.

The SCE electrode was connected to the cell through a salt bridge filled with 1 M aqueous solution of KCl. The platinum auxiliary electrode was an 8–10 cm^2 flag which was separated through a ceramic frit in the case of the nonaqueous system in order to reduce contamination of the working compartment electrolytes.

2.1.1. Electrochemical deposition of TiO_2 films

Titanium dioxide layers were electrodeposited on the top of a platinum cylinder in the regime of cycling voltammetry (CV) from aqueous solutions of titanium(IV) oxalate complexes. These solutions were made by dissolving of $TiCl_3$ (Merck), $H_2C_2O_4{\cdot}2H_2O$ (cz.d.a. Chempur), KNO_2 (97% Lancaster) and NH_3 (25% cz.d.a. POCH) in a doubly distilled water. Sometimes solid KNO_2 was replaced by a 2 M NH_4NO_2 solution. $TiCl_3$ was reacted with atmospheric oxygen before use. All solutions were not deoxidized before electrodeposition. More detailed conditions are summarized in Table 1. The surface of the working electrode was set on about 0.02 cm^2 by putting a thermoshrinkable tube made from polyethylene on a Pt cylinder. In the result the working electrode was resembled to a disk electrode in the shape. The electrode was also pre-treated by polishing successively with 10, 3, 1, 0.3 μm (and 0.03 before the SEM investigations) Al_2O_3, sonicating in water for 10 min and electrochemical cleaning by potential cycling in 0.5 M sulphuric acid prior to use.

Samples of the oxide precursor, after the electrodeposition step, were finally annealing at 450 °C in air for 1 h (heating rate 10 °C min^{-1}).

The mass of the TiO_2 films was determined in separate experiments by dissolving the films in a known amount of an 18% HCl solution four times at least. The concentration of titanium was measured by the ICP method. Knowing exactly the titanium concentration and the volume of the solution, the mass of the active material on each platinum electrode was easily calculated. The thickness of the oxide layers was estimated on the assumption that obtained films have density of crystalline anatase, *i.e.* 4.83 g cm^{-3}.

The additional TiO_2 samples were also made for SEM investigations. They were coated with gold and viewed using a JEOL JMS-35 scanning electron microscope.

2.1.2. Electrochemical investigations of lithium ion intercalation

1 M $LiClO_4$ solution was prepared in ultrapure propylene carbonate (Huntsman) under inert atmosphere in the nitrogen (Messer 5.0, 99.999%) tent. To ensure better the electrolytes against moistening there was P_2O_5 placed in the tent. $LiClO_4$ (reagent Plus™, Aldrich) was dried at 140 °C under vacuum for 48 h before using. All measurements were carried out at 25 °C in the electrolytes purged with nitrogen and kept in the nitrogen tent. TiO_2 samples were investigating according the procedure described below.

Firstly, the samples were scanned few times in the potential window −0.6 to −2.8 V *vs.* Ag/Ag^+ to remove traces of water adsorbed on the surface of TiO_2 and then a first series of voltammetric curves was recorded starting from the highest scan rates (200, 175, 150, 125, 100, 75, 50, 37, 25, 17, 10, 5, 2.5, 1, 0.8, 0.6, 0.4, 0.2 and 0.1 mV s^{-1}). For the scan rates 200–5 mV s^{-1}, two or three cycles without distinct differences in the shape of the consecutive voltammograms were measured. The next step included impedance spectra measurements under the constant potential polarization conditions using the ac potential amplitude of 5 mV. Samples were equilibrated for 1 h at each potential step before starting collecting the spectra. The potential was changed from −1.0 to −2.6 V every 0.2 V. Electrochemical impedance spectroscopy (EIS) was carried out in the frequency range 2×10^5 to 4×10^{-3} Hz (AZ1, integration time: three cycles), 2×10^5 to 1×10^{-3} Hz (AZ2 and AZ4, integration time: three cycles) and 2×10^5 to 2×10^{-3} Hz (AZ5, AZ6 and AZ7, integration time: two cycles). The impedance analysis was done for the frequencies not higher than 2×10^4 Hz.

Table 1
Conditions of the electrodeposition process[a].

Sample	Composition of the solutions used to electrodeposition (mol dm^{-3})					T (°C)	Potential window (V)	Scan rate v (mV s^{-1})	Number of cycles
	$TiCl_3$	$H_2C_2O_4$	NH_3	KNO_2(*) or NH_4NO_2	pH				
AZ1	1.1×10^{-2}	2.3×10^{-2}	5×10^{-2}	1×10^{-1}(*)	4.3	25	−0.3 to −1.0	5	**15**
AZ2	1.1×10^{-2}	2.3×10^{-2}	5×10^{-2}	1×10^{-1}(*)	4.3	25	−0.3 to −1.0	5	**8**
AZ4	1.1×10^{-2}	2.3×10^{-2}	5×10^{-2}	1×10^{-1}(*)	4.3	25	−0.3 to −1.0	5	**2**
AZ5	$\mathbf{1.0 \times 10^{-2}}$	1.8×10^{-2}	3.7×10^{-2}	1×10^{-1}	4.07	25	−0.3 to −0.8	5	10
AZ6	$\mathbf{4.1 \times 10^{-3}}$	7.1×10^{-3}	1.5×10^{-2}	1×10^{-1}	4.08	25	−0.3 to −0.8	5	10
AZ6a	$\mathbf{4.1 \times 10^{-3}}$	7.1×10^{-3}	1.5×10^{-2}	1×10^{-1}	4.08	**5**	−0.3 to −0.8	5	10
AZ7	$\mathbf{4.1 \times 10^{-3}}$	7.1×10^{-3}	1.5×10^{-2}	1×10^{-1}	4.08	25	−0.3 to −0.8	**25**	50

[a] The bold letters indicate variables that were changed in the series.

Cycling stability testing by means of cycling voltammetry was also performed. 100 cycles at 5 mV s^{-1} was collected for the each potential window: −0.6 to −2.4, −0.6 to −2.6 and −0.6 to −2.8 V. Finally, the rating capacity of the samples was measured during galvanostatic charge/discharge experiments (chronopotentiometry, CHP) at the potential window −1.0 to −2.8 V. Each TiO_2 sample was electrochemically studied for 2 weeks.

2.2. Raman spectroscopy

Raman spectra of the thin layers of TiO_2 were obtained at room temperature using a Jobin Y-von Horiba spectrometer, model T 64 000. 90° backscattering geometry and a cooled in liquid nitrogen CCD detector were used. The films were illuminated by a Spectra Physics argon ion laser line at 514.5 μm with a power of 50 mW at the samples.

3. Results and discussion

3.1. Raman spectroscopy

Raman spectra of the two AZ5-like films after the thermal treatment at two different temperatures are shown in Fig. 1. The Raman spectrum characteristic for anatase is seen for the oxide film annealed at 600 °C. The bands at 144, 199, 400, 520 and 640 cm^{-1} evidence its anatase structure [18]. On the other hand, the spectrum of the sample heated at 450 °C is similar to that presented for the amorphous titanium(IV) oxide in [18]. The bands at 170 and 610 cm^{-1} are considered to be characteristic for the amorphous phase [19]. Therefore, one may conclude that our titanium(IV) oxide films annealed at 450 °C are mostly amorphous but containing some anatase crystallites evidenced in the Raman spectra by a distorted peak feature at 136 cm^{-1}. The detailed structural studies of the TiO_2 films will be presented in the additional report focused on the electrodeposition procedures.

3.2. Scanning electron microscopy

SEM images of the studied TiO_2 films featured open pores and crevices created in between nonregular spherical aggregates composed of smaller crystallites. The selected representative images

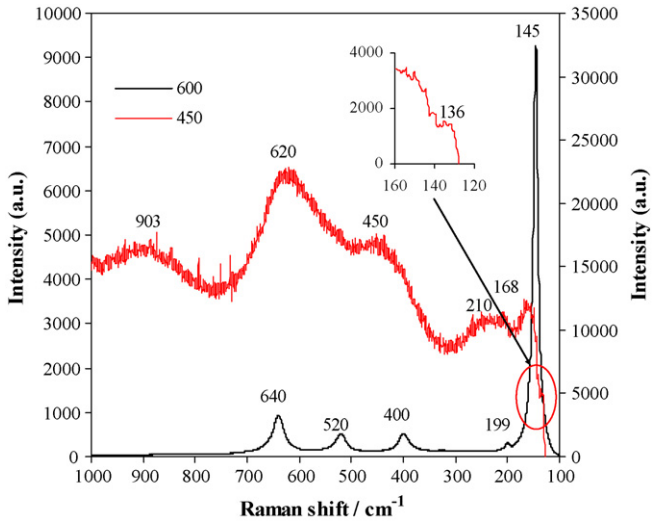

Fig. 1. Raman spectra of TiO_2 prepared at the conditions similar to that for the AZ5 film, annealed at 450 °C (red dash line) and 600 °C (black solid line). Inset: the spectrum in the range 120–160 cm^{-1} for the sample calcinated at 450 °C. (For interpretation of the references to color in this figure legend, the reader is referred to the web version of the article.)

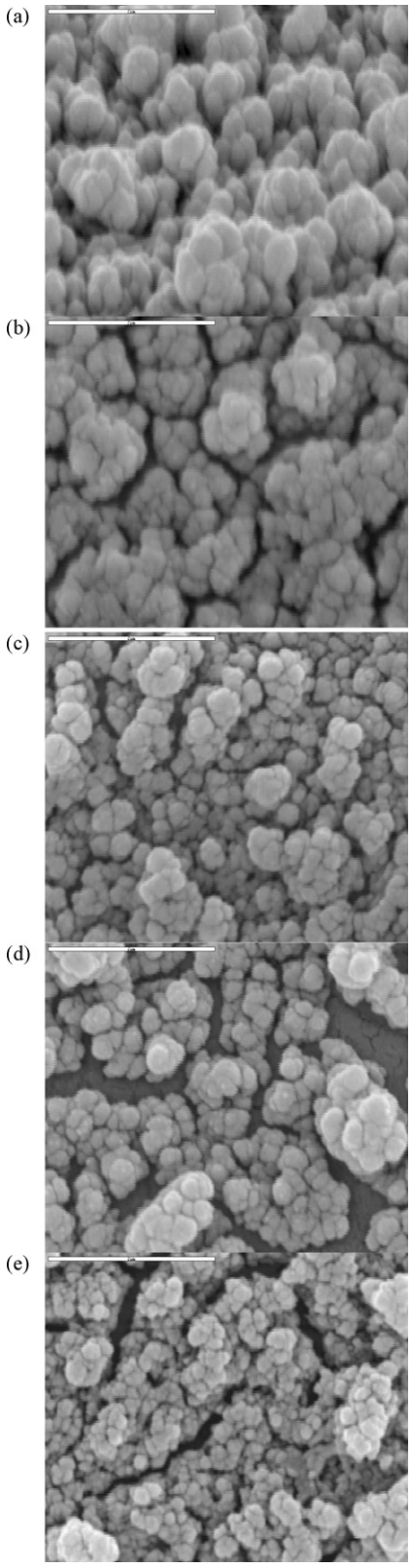

Fig. 2. SEM images for film AZ1 (a), AZ5 (b), AZ6 (c), AZ6a (d) and AZ7 (e); white labels = 2 μm.

(magnification 30,000×) of the surface morphology of the different films annealed at 450 °C are shown in Fig. 2. Mean sizes of the aggregates and the crystallites were calculated from the pictures of Fig. 2 using ImageJ 1.40 g and the results are shown in Table 2.

Table 2
Mean sizes of crystallites and aggregates determined from the SEM images shown in Fig. 2. Numbers of counts are shown in the parentheses.

Sample	Diameter (nm)	
	Aggregate	Crystallite
AZ1	568 (28)	152 (100)
AZ5	634 (40)	115 (103)
AZ6	337 (54)	71 (100)
AZ6a	523 (37)	120 (100)
AZ7	221 (64)	51 (102)

Electrochemical methods allow easy control of the morphology of the deposit by means of a control of the electrical variable of the reaction cell. The decrease of Ti(IV) concentration and the increase of the polarization rate result in the more nanostructural and higher ordered oxide films (the case of AZ6 and AZ7 samples). It would be of importance to decrease temperature of the oxide precursor deposition to avoid the fast decomposition of NH_4NO_2 in solution at the room temperature and to obtain the more nanostructural TiO_2 deposit on the electrode. Moreover, the more compact films are usually observed at the platinum side of the oxide deposits as seen in Fig. 2d.

3.3. Electrochemical studies

3.3.1. Cyclic voltammetry

Amorphous titanium(IV) oxide is known to intercalate Li^+ ions at electrode potentials from 0.5 to 0.6 V more negative than anatase [11]. In practice, to monitor intercalation, it requires the broader potential window in the negative direction to be available for Pt in the lithium electrolyte used in the study. The first scan cyclic voltammograms recorded at the scan rate 50 mVs^{-1} for a freshly cleaned polycrystalline Pt disc in 1 M $LiClO_4$-propylene carbonate solution are shown in Fig. 3. Although, on the thermodynamic basis, the reduction of propylene carbonate is predicted at about from −1.8 to −0.8 V (from 2 to 3 V *vs.* Li/Li^+), a significant increase in the reduction current is observed below about −2.6 V (1.2 V). The process is connected to the formation of the passive layer of lithium carboxylate ($ROCO_2Li$), which is transformed to Li_2CO_3 by water [20]. The negative limit potential was chosen as −2.8 V *vs.* Ag/Ag^+ in our measurements to minimize considerably the side reactions and, at the same time, to get the high intercalation degree.

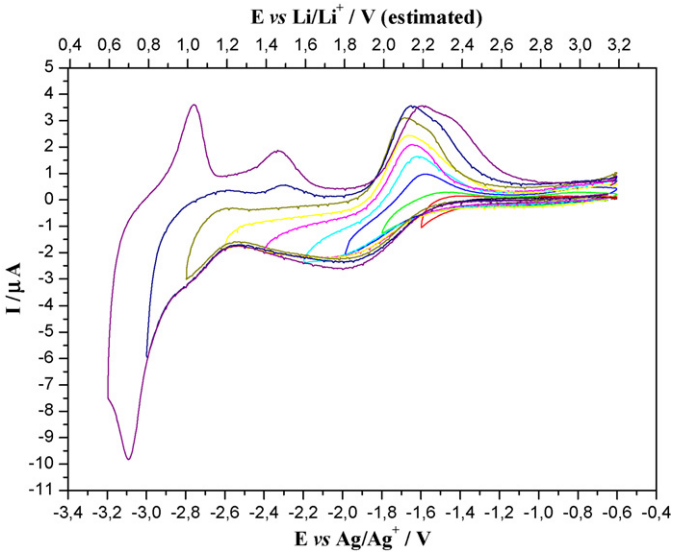

Fig. 3. Cyclic voltammograms recorded at 50 $mV\,s^{-1}$ for the freshly cleaned Pt disc (geometric surface area ≈ 0.02 cm^2) in 1 M $LiClO_4$-PC solution.

At about −2.0 V *vs.* Ag/Ag^+ one observes currents due to the reduction of the trace water. The anodic peaks at −2.8 V (1.0 V) and −2.4 V (1.4 V) were found also in [20]. The anodic peak at about −1.7 V, which is not observed at the Au electrode, the most probably originates from the reversible oxidation of H_2 on the Pt electrode.

The side reactions mentioned above are slower on TiO_2 than on Pt [14]. Moreover, the intercalation process may limit the competing side reactions considerably [12]. The representative CV-curves of the Li^+ inter/deintercalation process are shown in Fig. 4a and b.

The current tail, observed at potentials more negative than −2.5 V for the AZ6 film, does not occur for the more compact TiO_2 films (*e.g.* the AZ5 film). This feature can be a measure of the oxide film quality and the Pt blockade of the intervening side reactions on Pt by TiO_2. The observed anodic peak potentials are in accordance with the voltammetric behaviour of amorphous titanium(IV) oxide.

The mesoporous TiO_2 films are characterized by two pairs of the CV-peaks: (i) the first pair (1.75/1.95 V *vs.* Li/Li^+ at 0.1 $mV\,s^{-1}$) corresponds to anatase, (ii) the second pair (1.5/1.6 V *vs.* Li/Li^+ at 0.1 $mV\,s^{-1}$) corresponds to the amorphous phase and is described as the S-peaks due to their surface origin [11]. The TiO_2 films studied by us show the both pairs of peaks only at the slowest potential scan rates. The peaks of amorphous TiO_2 prevail in CV-curves at the higher scan rates. Such CV-characteristics indicates a low degree of crystallinity of our oxide films. The conclusion derived from CV-curves agrees well with Raman spectroscopy results.

Furthermore, the amorphous nature of the oxide phase can be confirmed on the basis of the quantitative analysis. The CV-peak currents should follow the linear dependence on the potential scan rate in this case (see Fig. 4c). On the other hand, the anatase peak currents follow the linear dependence on the square root of the potential scan rate indicating the diffusion control of the process even for the films as thin as 88 nm [21]. The corresponding analysis of the experimental data for the representative TiO_2 film is shown in Fig. 4c. The results might point out the prevailing intercalation of Li^+ into the surface states and/or high values of the diffusion coefficients of Li^+ in the final space of TiO_2 film. As a result the pseudo-capacitive behaviour is observed for the intercalation/deintercalation currents.

The reversibility of the intercalation process was measured by means of the anodic charge to the cathodic charge ratio, calculated by the integration of the corresponding voltammograms. Effects due to sizes of the crystallites on the reversibility of the intercalation process are shown in Fig. 4d. An increase of the reversibility is observed when the crystallites are getting smaller. However, at the longer time scales (at the lower scan rates where parasitic reactions and/or Li^+ diffusion in the oxide can be of a higher importance) one sees a transitional decrease in the reversibility of the intercalation that is accompanied by a drop in the capacity of the oxide films. Only the thinnest film, AZ7, degraded during the first performance cycle due, the most probably, to the side reactions at a Pt surface uncovered by TiO_2. For that reason only the AZ5 and AZ6 electrodes were subjected to the further quantitative analysis in this work.

The values of characteristic parameters of the AZ5 and AZ6 electrodes are shown in Fig. 5. The specific capacity was determined from the anodic part of the voltammograms (see Fig. 5a). The *b*-parameter is defined in the analytical equation (3) between current, *I*, and scan rate, *v*. The *b*-values calculated from the experimental current–potential curves recorded at *v* ranging from 1 to 100 $mV\,s^{-1}$ are shown in Fig. 5b. The *b*-values equal 0.5 and 1.0 are predicted for the processes of the semi-infinitive diffusion and the capacitive-like behaviour, respectively [2].

$$I = av^b \tag{3}$$

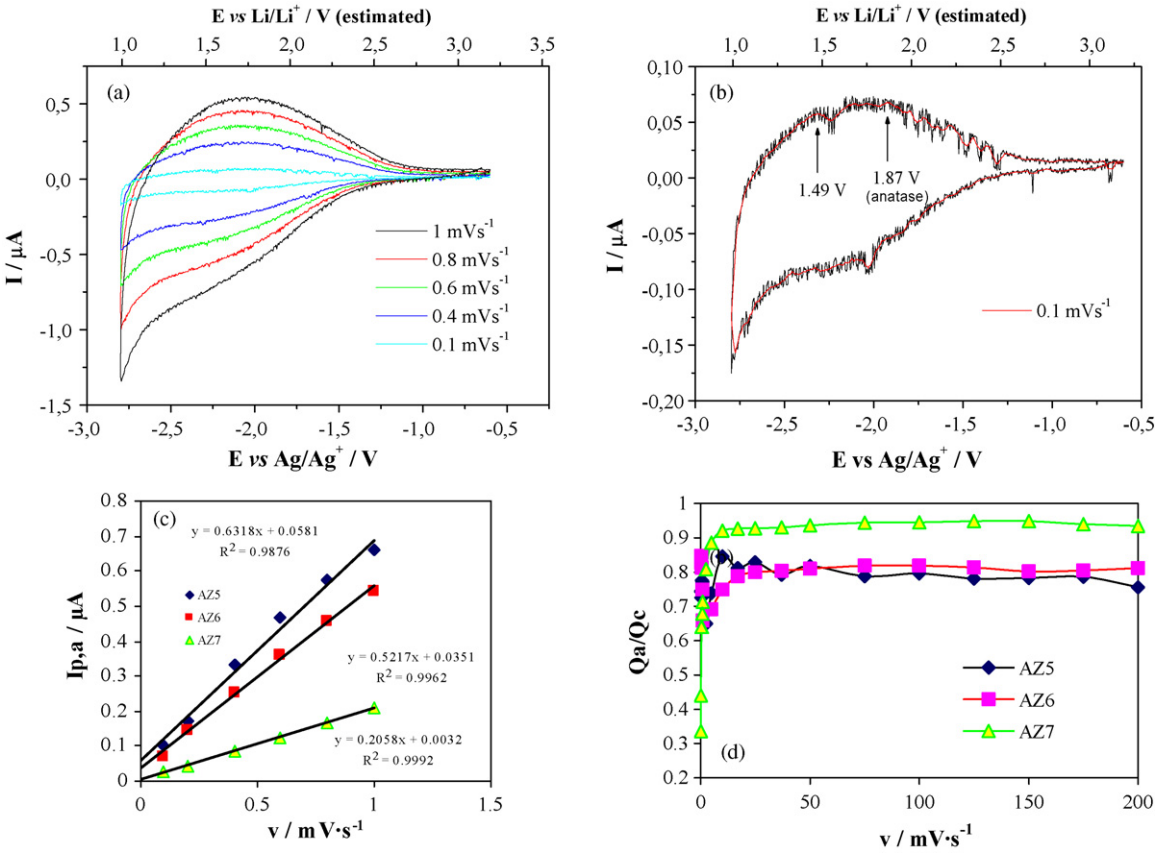

Fig. 4. The representative CV-data for inter/deintercalation of Li^+ in the TiO_2 films; (a) and (b) correspond to the AZ6 film. Details on (c) and (d) in the text.

A decrease of the Li^+ diffusion path lengths in the TiO_2 structures is found to improve significantly the reversibility of the intercalation process. Moreover, the fast surface processes are very important for observing the high specific capacity under the fast charging/discharging of the TiO_2 electrodes. Our results on the structure related ion transport and accumulation properties of TiO_2 confirm the results reported by other authors [10].

Stability of the TiO_2 films was studied under the CV conditions. Representative experimental data are shown in Fig. 6. The increase in the current and the cycling stability with the number of the scans is seen. It can be due to the partial irreversibility of the Li^+ intercalation (see Fig. 4d) resulting in an increase of the electronic conductivity of the oxide. Note that the good stability of our films concerns a broader potential range and a longer time scale than studied by other authors. Also, the stability is a much better than that reported in the literature for the amorphous TiO_2 films [17].

3.3.2. *Galvanostatic redox cycling*

Chronopotentiometric measurements confirm the amorphous structure of the studied TiO_2. The results of the galvanostatic charging/discharging are shown in Fig. 7 for the AZ6 film. There, the values of the reversible specific capacity and charging rates ($1\,C = 168\,mAh\,g^{-1}$) are shown by vertical and horizontal arrows, respectively. The charging/discharging curves slope continuously with a change in the lithium content in the TiO_2 layer for the entire potential range studied. This behaviour coincides with the shape

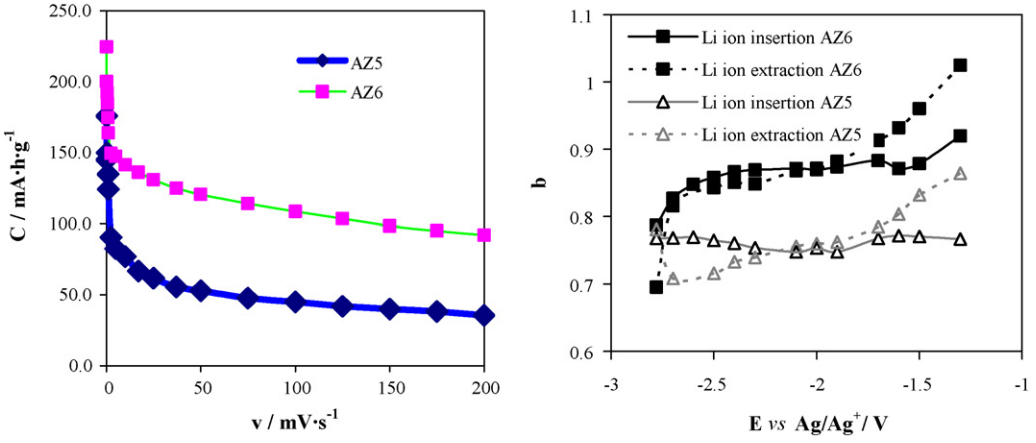

Fig. 5. Specific capacities and b-parameters of Eq. (3) determined from the CV-data for AZ5 and AZ6 films.

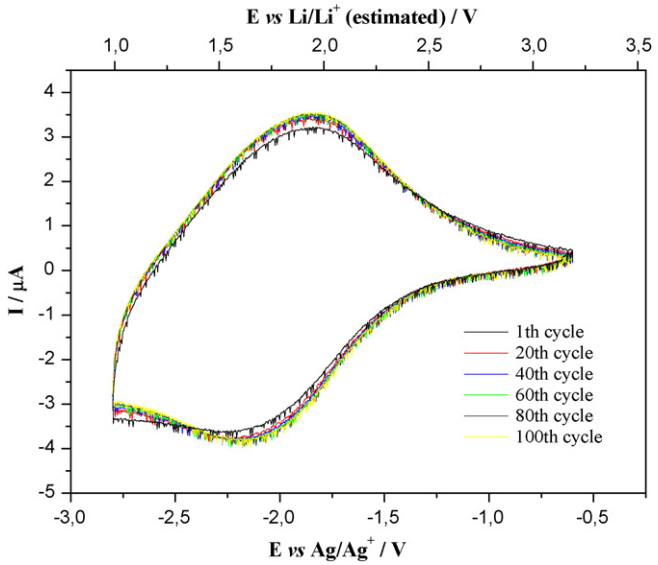

Fig. 6. Cyclic voltammograms of the AZ5 film – the cycling stability testing at potential scan rate 5 mV s^{-1}.

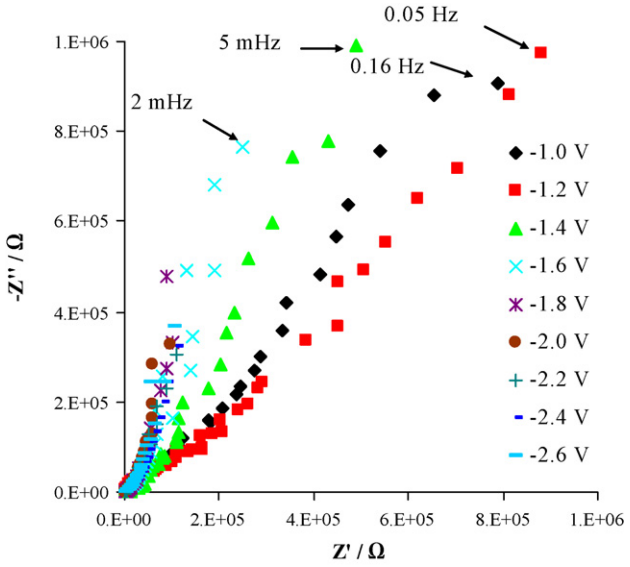

Fig. 8. The complex-plane impedance for AZ6 in 1 M $LiClO_4$-PC.

of the voltammograms which are characterized by the very broad peaks. An absence of the plateau on the charging/discharging curves indicates that the intercalation/deintercalation process does not change the structure of the host oxide phase.

The similar results were reported for hydrogen titanate [22], $K_2Ti_8O_{17}$ [23], TiO_2-B [24] and amorphous TiO_2 [16]. The Li^+ intercalation shows the pseudo-capacitive nature for the all above-mentioned material. On the other hand, anatase intercalates/deintercalates Li^+ in the stepwise process resulting in the two oxide phases which differ in the lithium content [25–27]. The characteristic plateau is seen in the galvanostatic charging/discharging curves in that case. A similar behaviour was found, for example, in $Li_4Ti_5O_{12}$ [28]. However, it should be noted that nanostructural anatase was shown to intercalate/deintercalate Li^+ through the process characterized by the sloppy parts in the charging/discharging curves, resembling the amorphous oxide behaviour [10].

The reversible capacity of the studied TiO_2 films was found stable on several cycles of the charging/discharging. A decrease in the value of this parameter was observed only during the very initial intercalation/deintercalation cycles. Nevertheless, the values of the capacity were found similar to that reported for TiO_2 mixed with conductive additives [16]. The highest value of the capacity, 160 mAh g^{-1}, was found for the AZ5 film at the low cycling rate 0.5 C. However, a further decrease of the cycling rate, to 0.2 C, increases a contribution of the side reactions in the observed electrode process.

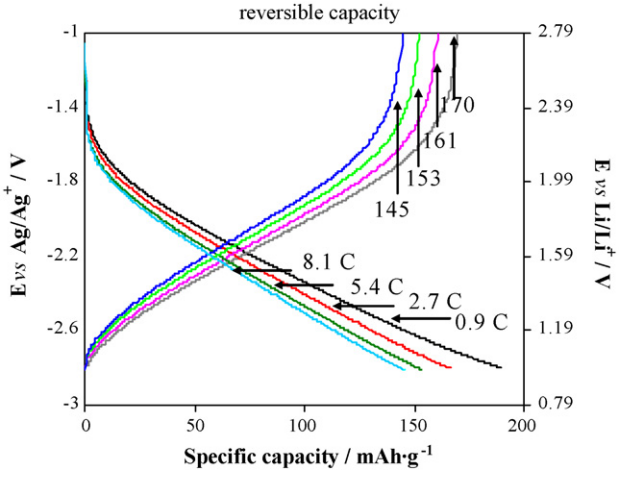

Fig. 7. Galvanostatic charge/discharge curves at the different C-rates for the film AZ6.

3.3.3. *Impedance studies*

The thin film TiO_2 electrodes were subjected to the impedance analysis. Two series of measurements were undertaken to show effects due to the film thickness and the film morphology. The representative experimental data in the impedance plane format are shown in Fig. 8 for the AZ6 film. In general, the shapes of the spectra are similar to that observed for the thin film electrodes of other electroactive materials, for example other transition metal oxides [29]. The high frequency depressed semicircle, the middle frequency line with the slope about 1, and the low frequency line with the slope much higher than 1 but not the vertical one (slope = ∞), are observed in the spectra. In the most cases, a clear change in the slope of the middle–low frequency spectra is seen, indicating the final space diffusion process in the TiO_2 films [30].

The equivalent electrical circuit model worked out by us and used in the subsequent quantitative analysis was $R_0(Q_1(R_1(Q_2T)))$ shown in Fig. 9 (see [31] for the notation).

The best quality fittings of the simulated and experimental data were obtained with this circuit. The other circuits, that were tested for the data fitting, were as follows: $R(Q(RW))C$, $R(Q(R(OC))$, $R(Q(RT))$. In the circuit description R, C, Q, W, O, and T elements represent resistance, capacitance, constant phase element, Warburg impedance, finite length diffusion impedance, and finite space dif-

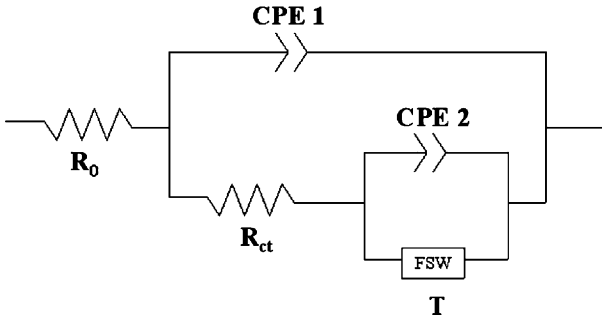

Fig. 9. Equivalent circuit used to data fitting.

Table 3
Parameters of the equivalent circuit $R_0(Q_1(R_1(Q_2T)))$ for TiO_2 samples at different potentials in 1 M $LiClO_4$-PC.

E (V)	R_0 (Ω)	$Q_{0,1}$	n_1	R_1	$Q_{0,2}$	n_2	$Y_{0,T}B$ (F)	B ($s^{0.5}$)	χ^2
AZ1									
−1.8	554	1.50E−05	0.71	9.63E+02	1.43E−05	0.73	6.50E−06	1.0	1.18E−03
−2.2	543	2.47E−05	0.66	2.67E+03	1.27E−05	0.70	8.06E−06	1.3	7.31E−04
−2.6	536	2.22E−05	0.63	3.12E+03	1.27E−05	0.68	9.16E−06	2.1	5.09E−04
AZ2									
−1.8	623	8.66E−06	0.69	5.69E+03	1.49E−05	0.73	6.72E−06	1.5	1.64E−03
−2.0	607	5.73E−06	0.72	4.05E+03	2.66E−05	0.71	1.28E−05	2.1	8.91E−04
−2.2	598	4.20E−06	0.74	3.96E+03	2.89E−05	0.68	1.65E−05	2.3	1.03E−03
−2.4	608	2.63E−06	0.77	3.97E+03	2.34E−05	0.63	1.82E−05	2.1	1.47E−03
−2.6	592	2.78E−06	0.76	3.11E+03	2.18E−05	0.65	2.01E−05	2.7	1.12E−03
AZ4									
−1.8	473	3.12E−06	0.72	7.75E+03	8.06E−06	0.70	9.9E−07	0.5	6.43E−03
−2.0	453	3.34E−06	0.71	1.25E+04	8.28E−06	0.69	3.46E−06	2.4	8.67E−04
−2.2	422	4.06E−06	0.66	1.56E+04	7.93E−06	0.67	5.78E−06	2.7	3.41E−03
−2.4	398	2.49E−06	0.68	1.16E+04	9.56E−06	0.64	5.20E−06	**2.1**	8.51E−03
−2.6	422	1.07E−06	0.75	6.89E+03	8.87E−06	0.60	1.06E−05	**2.1**	3.05E−03

fusion impedance (FSW), respectively [31]. The physical meaning of the circuit elements in the fitting model are as follows: R_0 is the electrolyte resistance, R_1 is reported as the charge transfer resistance at the oxide/electrolyte interface and/or the bulk film resistance [32], Q_1 represents the double layer impedance of the porous electrode, Q_2 and T connected in parallel represent the intercalation process of Li^+ to the surface states (predominantly for the small oxide crystallites) and to the bulk of the oxide (predominantly for the large oxide crystallites). The later points out the heterogeneous morphology of our TiO_2 films which is featured in a rather broad size distribution for the pores and the crystallites. In addition, element Q_2 may be related to the side reactions competing with the intercalation/deintercalation at the TiO_2/electrolyte interface.

The finite space diffusion element is represented by Eq. (4) [30,31]:

$$Z_T = {Y_{0,T}}^{-1}(j\omega)^{-1/2}\coth(B(j\omega)^{-1/2}) \quad (4)$$

where $j = \sqrt{-1}$ and ω is the angular frequency of the ac signal. The $Y_{0,T}$ and B parameters are related to the diffusion coefficient of the species that is transported in the finite space. The diffusion coefficient of Li^+ ions, D, was calculated from Eq. (5) [31,33]:

$$D = L^2B^{-2} \quad (5)$$

where L is the thickness of the finite diffusion space.

The values of the parameters found from the CNLS fitting of the experimental data with the equivalent circuit shown in Fig. 9, using EQUIVCRT.PAS v. 4.51 [31], are collected in Tables 3 and 4. The values of the diffusion coefficients calculated using Eq. (5) are included in Table 4.

The thicknesses of the films were estimated based on the ICP measurements and then used to calculate the D_{th}-values. The average diameters of the crystallites were found from the SEM analysis and then used to calculate the D_{cr}-values. The important finding concerns the diffusion rate parameter B observed for the AZ1, AZ2 and AZ4 films. The B-values seem to be independent on the total thicknesses of the films electrodeposited under the conditions leading to the similar diameters of their crystallites. The results might indicate that the Li^+ diffusion rate in the porous TiO_2 film is not controlled by the total thickness of the film but rather by the crystallite size and its distribution as well. The above conclusion is

Table 4
Parameters of the equivalent circuit $R_0(Q_1(R_1(Q_2T)))$ and the calculated D-values of Li^+ diffusion calculated on the basis of the crystallite size, D_{cr}, and the total film thickness, D_{th}, for the TiO_2 samples at different potentials in 1 M $LiClO_4$-PC.

E (V)	R_0 (Ω)	$Q_{0,1}$	n_1	R_1	$Q_{0,2}$	n_2	D_{cr} ($cm^2\ s^{-1}$)	D_{th} ($cm^2\ s^{-1}$)	C_L ($F\ g^{-1}$)	$Y_{0,T} \times B$ (F)	B^2 (s)	χ^2
AZ5 (1.689 μg, calculated thickness: 219 nm, crystallite diameter: 152 nm)												
−1.4	537	6.57E−06	0.61	4.30E+03	1.03E−05	0.74	–	–	–	–	–	4.08E−03
−1.6	476	1.54E−05	0.55	3.08E+03	1.90E−05	0.75	2.9E−12	6.0E−10	2	3.09E−06	0.8	9.59E−03
−1.8	505	1.60E−05	0.59	1.87E+03	3.22E−05	0.68	3.4E−14	7.9E−12	22	3.67E−05	61.0	5.15E−04
−2.0	499	2.32E−05	0.55	1.94E+03	2.94E−05	0.73	5.0E−14	1.0E−11	39	6.55E−05	46.6	3.11E−04
−2.2	499	2.51E−05	0.55	1.98E+03	2.49E−05	0.75	4.6E−14	9.5E−12	38	6.44E−05	50.4	5.36E−04
−2.4	505	2.52E−05	0.55	2.09E+03	1.71E−05	0.78	3.8E−14	7.8E−12	28	4.76E−05	61.2	4.92E−04
−2.6	512	1.92E−05	0.58	1.19E+03	1.70E−05	0.79	1.1E−14	2.4E−12	42	7.07E−05	201.6	2.75E-03
AZ6 (1.001 μg, calculated thickness: 130 nm, crystallite diameter: 71 nm)												
−1.4	415	4.18E−08	0.88	6.45E+03	2.33E−06	0.45	8.7E−14	2.9E−11	15	1.49E−05	5.8	9.43E−03
−1.6	599	7.40E−06	0.57	5.68E+03	3.55E−06	0.65	7.2E−14	2.4E−11	44	4.37E−05	7.02	4.04E−03
−1.8	538	1.12E−05	0.62	1.89E+03	8.75E−06	0.62	4.9E−14	1.7E−11	93	9.31E−05	10.2	3.19E−03
−2.0	520	1.09E−05	0.63	1.09E+03	1.58E−05	0.61	3.8E−14	1.3E−11	125	1.25E−04	13.4	3.21E−03
−2.2	515	1.48E−05	0.61	1.36E+03	1.73E−05	0.62	3.6E−14	1.2E−11	107	1.07E−04	14.0	9.37E−04
−2.4	509	1.50E−05	0.60	1.18E+03	1.12e−05	0.59	2.7E−14	8.9E−12	112	1.12E−04	18.9	8.77E−04
−2.6	497	1.38e−05	0.59	8.21E+02	4.99e−06	0.57	3.4E−14	1.1E−11	123	1.23E-04	15.0	2.49E-03
AZ7 (crystallite diameter: 51 nm)												
−1.8	564	6.37E−06	0.69	1.31E+03	1.36E−05	0.75	6.8E−14	–	–	2.61E−05	3.8	3.47E−03
−2.0	554	4.60E−06	0.74	8.26E+02	1.65E−05	0.79	4.9E−14	–	–	5.01E−05	5.3	7.63E−03
−2.2	538	6.58e−06	0.71	8.64E+02	1.59E−05	0.77	5.8E−14	–	–	4.52E−05	4.5	3.98E−03
−2.4	521	6.48E−06	0.70	1.02E+03	1.24E−05	0.74	6.2E−14	–	–	4.28E−05	4.2	5.11E−03
−2.6	517	5.16E−06	0.71	8.78E+02	1.10E−05	0.74	5.9E−14	–	–	4.18E−05	4.4	4.50E−03

supported by our results on the charge accumulation capacitance, C_L, of the TiO_2 films. The C_L-values were calculated from the parameters of the impedance fitting function using the formula $C_L = Y_{0,T}B$ [31,33]. The C_L-values correlate with the film thickness as expected for the parameter being a measure of the total quantity of the oxide undergoing the inter/deintercalation process. Therefore, the D_{cr} coefficient seems to be a more reliable diffusion rate parameter than the D_{th} coefficient for the all studied TiO_2 films.

The effective Li^+ diffusion distance, δ, calculated according to Eq. (6), assuming $D = 5 \times 10^{-14}$ cm^2 s^{-1} and the time period 1 s, is 4 nm.

$$\delta = \sqrt{\pi D t} \quad (6)$$

The δ-value is found smaller than the diameters of the crystallites observed in the TiO_2 films. Thus, one might expect to increase the specific capacity of the oxide material by a decrease of the size of the crystallites. On the other hand, the determined D_{cr}-values, within the experimental error range, can be considered as independent on the crystallite size. Note, that the D_{th}-values are found three orders of the magnitude higher than the D_{cr}-values. Moreover, the calculated D_{th}-values can be considered as underestimated due to the usually underestimated thickness of the porous films.

The D-values reported in the literature for anatase are: 2×10^{-15} to 1×10^{-18} [12], 1×10^{-17} to 7×10^{-17} [2,34], 2×10^{-14} to 6×10^{-14} [21], all quoted in cm^2 s^{-1}. Diffusion of Li^+ in amorphous TiO_2 is, the most probably, faster than in anatase. For example, $D = 3 \times 10^{-15}$ for amorphous and $D = 1 \times 10^{-17}$ to 4×10^{-17} cm^2 s^{-1} for anatase TiO_2 were reported in [11]. Interestingly, our TiO_2 films are characterized by the diffusion coefficients of the order of 10^{-14} cm^2 s^{-1} (calculated as D_{cr}). Furthermore, the D-values determined in this work are found to decrease with the increase of a degree of the Li^+ intercalation. The similar behaviour was reported in the literature and may be considered as due to the repulsive interactions between lithium ions in the oxide matrix [12].

4. Conclusions

The new electrodeposition method for the thin TiO_2 films on platinum was developed. The film quality, quantity and morphology depend on: (i) rates of changes in pH of the solution near the Pt surface, (ii) rates of decomposition of the titanium(IV) oxalate complexes, (iii) rates of the follow-up condensation reactions of the oxide precursor on platinum. The processes were found to be easy controlled with the cyclic voltammetry method. The potentiodynamic regime allows for a more effective control of the deposition and intercalation/deintercalation processes through the potential scan rate parameter.

The TiO_2 films with the average crystallites diameter 51 nm were deposited from the solution containing the lowest concentration of Ti(IV) oxalate complexes and the method can be optimized further. Amorphous TiO_2 obtained at 450 °C shows the good intercalation properties and the controllable morphology. The electrochemically produced thin TiO_2 films do not reveal the pure pseudo-capacitive behaviour. The Li^+ intercalation/deintercalation is therefore not constrained only to the surface redox processes of the oxide. The diffusion process of Li^+ was found to take place under conditions of the finite volume/space. The diffusion rate seems to be controlled by the dimensions of the crystallites and the total thickness of the film being of minor importance for the D-value. The Li^+ diffusion coefficients of the order of 10^{-14} cm^2 s^{-1} seem to be the most reliable values for the studied predominantly amorphous TiO_2 films.

Reversibility of the observed intercalation process decreased when the sizes of the crystallites increased. Therefore, the surface processes appeared to be decisive for the high coulombic efficiency and high rate performance of lithium ion battery. The results of our CV, CHP and EIS studies were found selfconsistent. However, the selfdischarge of the TiO_2 films was found under OCP but an origin of this process is not recognized yet.

References

[1] G. Boschloo, D. Fitzmaurice, J. Phys. Chem. B 103 (1999) 7860–7868.
[2] H. Lindström, S. Södergren, A. Solbrand, H. Rensmo, J. Hjelm, A. Hagfeldt, S.-E. Lindquist, J. Phys. Chem. B 101 (1997) 7717–7722.
[3] P. Bonhôte, E. Gogniat, M. Grätzel, P.V. Ashrit, Thin Solid Films 350 (1999) 269–275.
[4] P.G. Bruce, Solid State Ionics 179 (2008) 752–760.
[5] C. Natarajan, F. Fukunaga, G. Nogami, Thin Solid Films 322 (1998) 6–8.
[6] I. Exnar, L. Kavan, S.Y. Huang, M. Grätzel, J. Power Sources 68 (1997) 720–722.
[7] C.M. Wang, S.Y. Lin, J. Solid State Electrochem. 10 (2006) 255–259.
[8] I. Moriguchi, R. Hidaka, H. Yamada, T. Kudo, Solid State Ionics 176 (2005) 2361–2366.
[9] H. Yamada, T. Yamato, I. Moriguchi, T. Kudo, Solid State Ionics 175 (2004) 195–198.
[10] Ch. Jiang, M. Wei, Z. Qi, T. Kudo, I. Honma, H. Zhou, J. Power Sources 166 (2007) 239–243.
[11] L. Kavan, J. Rathousky, M. Grätzel, V. Shklover, A. Zukal, J. Phys. Chem. B 104 (2000) 12012–12020.
[12] D. Fattakhova, L. Kavan, P. Krtil, J. Solid State Electrochem. 5 (2001) 196–204.
[13] R. Armstrong, G. Armstrong, J. Canales, R. García, P.G. Bruce, Adv. Mater. 17 (2005) 862–865.
[14] L. Kavan, K. Kratochvilová, M. Grätzel, J. Electroanal. Chem. 394 (1995) 93–102.
[15] J. Yan, H. Song, S. Yang, J. Yan, X. Chen, Electrochim. Acta 53 (2008) 6351–6355.
[16] M. Hibino, K. Abe, M. Mochizuki, M. Miyayama, J. Power Sources 126 (2004) 139–143.
[17] S. Karuppuchamy, M. Iwasaki, H. Minoura, Appl. Surf. Sci. (2006) 2924–2929.
[18] P. Kern, P. Schwaller, J. Michler, Thin Solid Films 494 (2006) 279–286.
[19] A. Niilisk, M. Moppel, M. Pärs, I. Sildos, T. Jantson, T. Avarmaa, R. Jaaniso, J. Aarik, CEJP 4 (2006) 105–116.
[20] D. Aurbach, M. Daroux, P. Faguy, E. Yeager, J. Electroanal. Chem. 297 (1991) 225–244.
[21] M.J. Lindsay, M.G. Blackford, D.J. Attard, V. Luca, M. Skyllas-Kazacos, C.S. Griffith, Electrochim. Acta 52 (2007) 6401–6411.
[22] J. Li, Z. Tang, Z. Zhang, Chem. Phys. Lett. 418 (2006) 506–510.
[23] B.L. Eang, Q. Chen, J. Hu, H. Li, Y.F. Hu, L.-M. Peng, Chem. Phys. Lett. 406 (2005) 95–100.
[24] T. Brousse, R. Marchand, P.-L. Taberna, P. Simon, J. Power Sources 158 (2006) 571–577.
[25] J. Xu, Y.Y. Wang, Z. Li, W.F. Zhang, J. Power Sources 175 (2008) 903–908.
[26] R. van de Krol, A. Goossens, J. Schoonman, J. Phys. Chem. B 103 (1999) 7151–7159.
[27] A. Henningsson, M.P. Andesson, P. Uvdal, H. Siegbahn, A. Sandell, Chem. Phys. Lett. 360 (2002) 85–90.
[28] Y.H. Rho, K. Kanamura, J. Solid State Chem. 177 (2004) 2094–2100.
[29] S.-I. Pyun, J.-S. Bae, Electrochim. Acta 41 (1996) 919–925.
[30] B. Rodgers, Research Solution & Resources for Electrochemistry, 2008, http://www.consultrsr.com/index.htm.
[31] B.A. Boukamp, Eqivalent Circuit (equivcrt.pas) Users Manual, second ed., University of Twente, 1989.
[32] H. Sato, D. Takahashi, T. Nishina, I. Uchida, J. Power Sources 68 (1997) 540–544.
[33] B. Więcek, U. Twardoch, J. Phys. Chem. Solids 65 (2004) 263–268.
[34] Z. Liu, L. Hong, B. Guo, J. Power Sources 143 (2005) 231–235.